Microcharacterization of Interface Oxide Layer on Laser-Structured Silicon Surfaces of Plated Ni–Cu Solar Cells

Andreas Büchler, Benjamin Grübel, Varun Arya, Tobias Weingärtner, Angelika Hähnel, Volker Naumann, Jonas Bartsch, Markus Glatthaar, and Sven Kluska

***Abstract*—Light-induced plating on laser-structured passivation layer openings is an alternative method to silver screen printing for fabrication of the front-side metal grid on silicon solar cells. Fundamental contact properties, such as adhesion and contact resistance, are determined at the highly inhomogeneous interface of laser-structured silicon and plated nickel. Usage of laser structuring and plating holds the risk that an interfacial oxide layer is incorporated to the contact stack. It is shown within this article that both native and laser-induced oxide formation influence contact properties. Although, a native oxide layer does not impede metal deposition during plating, the dynamics of the layer formation is shown to be changed. It is known that interface oxides harm the contact resistance, and it is reported that postplating annealing decreases the contact resistance. In this article, the microstructural basis of the temperature-induced changes is examined. By transmission electron microscopy and energy dispersive X-ray spectroscopy, no temperature-induced modification of the interface microstructure, such as silicide formation or metal-induced crystallization of the amorphous surface, is observed. Results suggest that the decrease is attributed to a temperature-induced change of the electrical properties of the interface oxide. Considering reports that partially closed interface oxide layers are an inherent feature of laser-structured plated contacts, the results presented motivate reconsidering the objective of postplating annealing. The results indicate that the beneficial impact of silicide formation is overrated for the case of laser-structured plated contacts, whereas the temperature-induced modifications on residual interface oxide layers are neglected in the scientific discussions on the given contact stack.**

***Index Terms*—Photovoltaic cells, semiconductor device reliability, semiconductor-metal interfaces, silicidation.**

This work was supported by the German Federal Ministry for the Economic Affairs and Energy under Groschen Project No. FKZ: 0324012 and Genesis Project No. FKZ: 032474. *(Corresponding author: Andreas Büchler.)*

A. Büchler, B. Grübel, V. Arya, J. Bartsch, M. Glatthaar, and S. Kluska are with the Fraunhofer Institute for Solar Energy Systems, Freiburg 79110, Germany (e-mail: andreas.buechler@posteo.de; benjamin.gruebel@ise.fraunhofer.de; varun.arya@ise.fraunhofer.de; jonas.bartsch@ise.fraunhofer.de; markus.glatthaar@ise.fraunhofer.de; sven.kluska@ise.fraunhofer.de).

T. Weingärtner is with the Institut für Angewandte Materialen, Karlsruher Institut für Technologie, Eggenstein-Leopoldshafen 76344, Germany (e-mail: tobias.weingaertner@kit.edu).

A. Hähnel and V. Naumann are with the Fraunhofer Center for Silicon Photovoltaics CSP, Halle 06120, Germany (e-mail: angelika.haehnel@csp.fraunhofer.de; volker.naumann@csp.fraunhofer.de).

I. Introduction

LIGHT-INDUCED plating enables self-aligned deposition of a nickel–copper–silver stack in laser-structured passivation layer openings of silicon solar cells [1]. This metallization approach holds the potential to significantly lower the material cost compared with silver screen printing. Recently, promising results have been obtained for Ni-/Cu-/Ag-plated aluminum back surface field (Al-BSF) and passivated emitter and rear (solar) cell (PERC) solar cells [2]–[6]. An industrially feasible front-side metallization sequence, which is also applied at Fraunhofer ISE, is consists of structured ablation of the passivation layer by a picosecond (ps)-pulsed UV laser, an hydrofluoric acid (HF) dip to remove native and laser-induced oxides within the passivation layer openings, plating of Ni ($\sim$1 μm), Cu ($\sim$9 μm), and Ag ($\sim$0.5 μm), and a subsequent contact formation annealing at temperatures in the range of 200–250 °C [7].

Several contact properties are determined by the interface properties of the metal–silicon interface formed via laser structuring and nickel plating. An appropriate surface topography within the passivation layer openings ensures mechanical stability in respect to finger and busbar adhesion even without formation of nickel silicide. Due to interference of incoming laser light and reflections of the pyramid textured front side, periodically ordered ripples (similar to laser-induced periodic surface structures [8]) occur during passivation layer ablation using a ps- or femtosecond-pulsed laser source. The ripples provide the roughness features that are necessary to adhesively key the plated layer onto the silicon surface [9].

The contact resistance of laser-structured plated contacts is reported to decrease during annealing the contact stack after plating at temperatures in the range of 200–450 °C. The temperature-induced effect is attributed to silicide formation. But, silicide formation from plated nickel on laser-structured silicon was shown to be impeded by interface oxides.

During the metallization sequence, the solar cell precursors are dipped into HF, rinsed, and immediately transferred to the nickel electrolyte. During the rinsing and the transfer to the electrolyte, an oxide layer regenerates [10]. Thus, plated contacts are expected to feature a shallow interfacial oxide layer. It is reported that the oxide is a barrier toward the formation of a continuous silicide layer during the postplating annealing [11]. In studies on plated layers within passivation layer openings created by the

chemical removal that does not modify the surface near silicon volume, the formation of homogenous nickel silicide layers has been reported. In contrast, in the context of plated contacts structured by pulsed UV-lasers, only singular island-like silicide structures are found. It is assumed that the positions of silicide formation at the interface of plated nickel and laser-structured silicon coincident with breaks of the interfacial oxide layer [10]. The influence of annealing on the interface oxides was not investigated yet.

Recently, Kluska *et al*. [12] suggested to omit the HF dip and incorporate the surface oxide into the plated contact. For nonoptimized antireflection coating (ARC), parasitic plating (also referred to background or ghost plating) occurs at ARC pinholes and harms the performance and the esthetics of the solar cells [13]–[15]. Skipping the oxide removal avoids parasitic plating, as defects of the passivation layer are electrically insulated by native oxides. It was shown that a nickel layer can be plated onto the oxidized passivation layer opening. This indicates that electron transport throughout the oxidize layer is possible. It was reported that the incorporated oxide impedes the contact resistance. But postplating annealing lowers the contact resistance drastically, although a formation of silicide was not detected [16].

In the following, the influence of interface oxide layers on the contact resistance of laser-structured plated contacts is investigated before and after postplating annealing. Results acquired on solar cell level are supplemented by results from microcharacterization. The influence of residual oxide layers on the plating process and the postplating annealing is examined. In particular, the composition, homogeneity, and thickness of a residual interface oxide are characterized before and after contact formation anneal. Results from Auger electron spectroscopy (AES) and a combination of transmission electron microscopy (TEM) and energy dispersive X-ray spectroscopy (EDXS) are considered. Furthermore, the influence of a residual oxide on the nuclei formation during the plating process is analyzed on the basis of scanning electron microscopy (SEM) images. Finally, the effect of contact formation annealing on the interface situation is examined.

Until now, the contact resistance decrease due to postplating annealing was attributed to silicide formation [17], [18]. Based on the results presented, silicide formation is excluded for contact stacks featuring a continuous interface oxide. Alternative mechanisms are discussed on the basis of the observations during microcharacterization.

II. Experimental Section

All experiments presented are performed on industrially manufactured p-type Czochralski-grown (Cz) monocrystalline Si Al-BSF solar cell precursors. The wafers were taken from the same supplier as in previous publications ([16] and material D in [15]). The precursors feature a screen-printed and fired backside metallization and a random pyramid textured front side with a thermally diffused phosphorous emitter that is passivated by a plasma enhanced chemical vapor deposition (PECVD) silicon nitride. The front-side metallization grid is structured by locally removing the passivation layer. Therefore, a ps-pulsed laser with a wavelength of 355 nm is used, which is operated at the passivation layer ablation threshold energy. In order to create line-like passivation layer openings for the finger contacts, a galvo-scanner moves the pulsed laser beam in a way that subsequent ablation dots are touching each other without significant overlapping of the final contact opening circles. The ablation configuration results in pearl-chain pattern, featuring closely space ablation dots with a diameter of approximately 12 μm. The HF dip and plating of Ni, Cu, and Ag are performed in single-side inline plating tools of the company Rena Technology GmbH. The nuclei formation in the first instances of nickel plating is investigated on samples fabricated in the same plating tool that is used for solar cell fabrication. Transport system and contact units are modified to allow nickel plating times of 1, 5, and 10 s. Postplating annealing is performed in an inline belt furnace, applying a temperature profile that features a plateau of 225 °C for 3 min under N_2 atmosphere.

Three types of contact stacks are considered, which differ in respect to the interface oxide layer. Group 1 is the reference group, Group 2 features a native oxide layer that is intentionally grown between HF dip and plating, and Group 3 features a laser-induced interface oxide layer.

Group 1 is fabricated by the reference process that includes an oxide removal step, by dipping the one side of wafers in 1%vol HF for 30 s immediately before Ni-plating. A cross-sectional study revealed an interface oxide of less than 2 nm that is not formed continuously [13]. According to the authors of the respective publication, the oxide is generated during rinsing and the transfer time in-between HF dip and nickel plating. The reported measured thickness, however, excides other published measurement values for the thickness of native oxides on n-type doped (111)-silicon wafers by a factor of ten [19]. For Group 2, a native oxide layer is intentionally grown after the HF dip. The wafers are stored for 10 min in ambient air before plating (as described in [16]). The storage time is expected to result in an increased oxide growth in respect to Group 1. Contacts of Group 3 feature a laser-induced interface oxide layer. Nickel is plated without an HF dip within 20 s after the laser ablation of the passivation layer. The resulting contacts is equal to *Easy Plating* contacts, as described by Kluska *et al.* [20]. The estimated thickness of a laser-induced oxide is in the range of 2–5 nm [21]. The experimental groups are summarized in Table I. For all groups, solar cells and nucleation samples are manufactured. All sample types were evaluated with and without postplating annealing.

For the characterization of the silicon surface after contact annealing and, in particular, for the analysis of silicide formation, unreacted nickel is removed selectively without harming nickel silicide using piranha etch [22]. For SEM, a Zeiss Auriga Cross Beam is used. AES was performed using a PHI 680 Xi Auger Nanoprobe that is operated at 10 kV and 10 nA and features a spatial resolution of 40 nm. The sputtering unit allows creating depth profiles of the elementary composition with a depth resolution of 0.5–2 nm. In order to suppress distortions due to the repeated measurement of sputtering debris that redeposits in the rough surface, the measurement positions were set on pyramid tips that represent local peaks in the topography of the passivation layer openings.

TABLE I
EXPERIMENTAL GROUPS

Group	Name	Metallization sequence of passivated phosphorous emitter
1	Reference	LCO HF-Dip Rinsing 2s transfer time Ni-Plating
2	Native oxide	LCO HF-dip Rinsing Storage in ambient air for 10 min Plating
3	Laser induced oxide	LCO 20 s transfer time Ni-Plating

LCO: Laser contact opening.

Lamellae samples were prepared for TEM investigations using a ZEISS Xradia 410 Versa. On each sample, the lamella was chosen at the same position in respect to the laser ablation pattern. Furthermore, the orientation of the lamella was strictly adjusted to the orientation of textured pyramids, to allow for a prediction of the material composition of the excited volume of the lamella from the cross section perspective. An FEI TecnaiG2 F20, equipped with a high-angle annular dark field (HAADF) detector and EDAX-Si(Li) EDX system, was used for the characterization based on TEM. Pointwise evaluation of the chemical composition acquired by subsequent EDXS measurements at different spots along a defined line allowed for measurements of EDXS profile lines. For each measurement position, the integral of X-ray emission from the whole excited volume is measured. The diameter of the excited volume in TEM measurements at high acceleration voltages is in the order of a few nanometer. Assuming sharp junctions in between the different layers and a smearing due to the extent of the excited volume, the EDXS profile is modeled and the parameters of the model, such as the thickness of the interfacial oxide layer, are adjusted until the modeled profile lines match the measurement data. The measurement configuration of the EDXS measurement is sketched in Fig. 1.

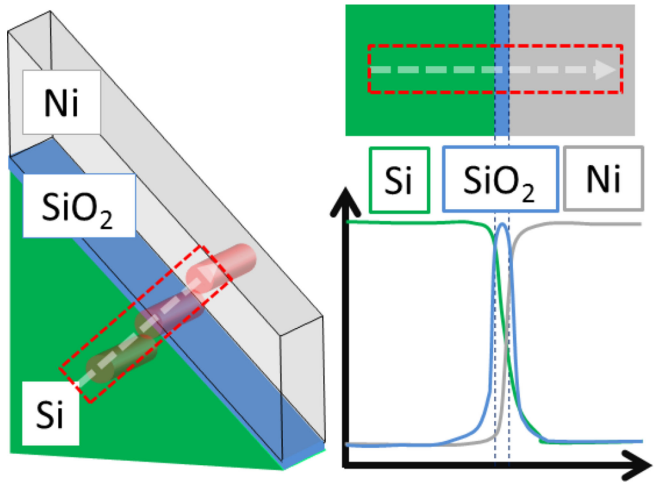

Fig. 1. Sketch of the orientation of the plated stack within the lamella in respect to texture geometry and excitation volume. Expected signal curves in energy dispersive spectroscopy (EDS) line scans along the interface: the sharp intersection smear due to the extent of the excitation volume.

TABLE II
ELECTRICAL CONTACT PROPERTIES

	Group	IV measurements			TLM
		Eta (%)	pFF (%)	Rs (Ωcm²)	ρ_c (mΩcm²)
1	w/o anneal	19.0	82.6	0.57	0.7 ± 0.1
	Annealed	19.2	82.2	0.46	0.6 ± 0.1
2	w/o anneal	18.9	82.7	0.71	19 ± 1
	Annealed	19.4	82.2	0.28	1.2 ± 0.2
3	w/o anneal	19.0	83.0	0.70	2.9 ± 0.7
	Annealed	19.1	82.4	0.53	1.5 ± 0.2

pFF: Pseudo fill-factor.

III. RESULTS

A. Postplating Annealing Significantly Decreases the Contact Resistance of Contacts With an Interface Oxide Layer

Table II summarizes the results of *IV* curve and transfer length method (TLM) measurements on samples of the three experimental groups that were fabricated with and without postplating annealing. V_{oc} and J_{sc} values were determined to be (633 ± 2) mV and (37.6 ± 0.2) mA/cm², respectively, and did not show a correlation with the estimated interface oxide status.

The presented results of the contact and series resistance values go along with previous publications [15], [16], [20]. Contacts featuring an intentionally incorporated oxide layer of presumably 2–5 nm are characterized by a significantly higher contact resistance (Group 2 and 3) compared with contacts immediately after an HF dip (Group 1), if contacts are fabricated without postplating annealing. Annealing after plating causes a significant drop in the resistance values on contacts with interface oxide. Thus, after postplating annealing, the influence of the interface oxide on the series resistance of solar cells is attenuated [23].

B. Presence of Interface Oxides Lowers the Density of Nuclei During the First Instance of Nickel Plating

For solar cell fabrication, usually a nickel layer with a thickness of ∼1 μm is plated as a stable diffusion barrier against copper. For the used plating settings, this thickness corresponds to a plating duration of 120 s. The SEM images in Fig. 2 show the thickness of the plated nickel layer after different plating times. Nickel was deposited on silicon surfaces equally prepared as the contact area of the solar cell samples. The images for shorter durations are taken from top view perspective. The lower row shows a cross-section of the contact after a nickel plating time of 120 s and subsequent copper plating. Within the experiment presented, no difference was observable regarding

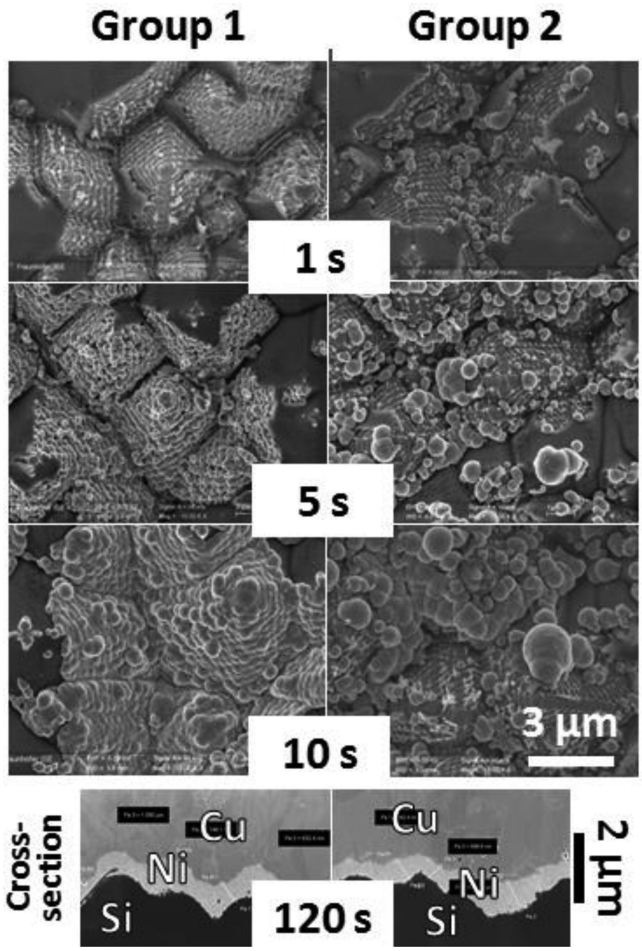

Fig. 2. SEM images from the top view perspective of the laser-structured passivation layer opening of samples at different plating times (1, 5, 10, and 120 s) with HF dip immediately before plating (Group 1, no interface oxide expected) and an expected native oxide on the Si surface due to a delay between HF dip and plating (Group 2).

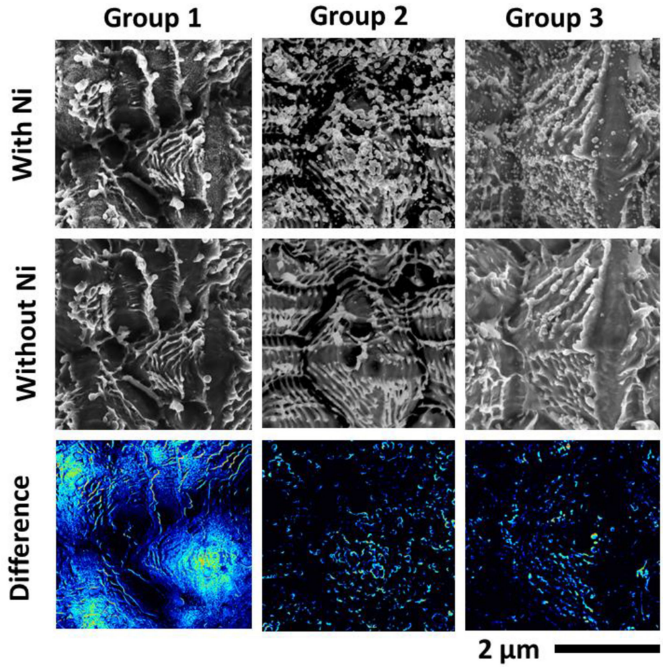

Fig. 3. SEM images after 1 s of nickel plating and after a subsequent removal of the metallization, and a false-color image that indicates the differences. Features in the false-color image indicate positions of the Ni nuclei in the images of the first row.

the appearance of the final nickel layer of samples from all three experimental groups. This highlights that the thickness of the nickel layer after 120 s is not sensitive to interface oxide layers. Thus, during the 120 s of plating, the same number of electrons is exchanged in-between silicon bulk and electrolyte throughout the solar cell surface on samples with and without superficial oxide layer. But the growth dynamics of the nickel layer differs significantly on samples with (Groups 2 and 3) and without (Group 1) superficial oxide layer. In particular, the density of nuclei during layer formation is different. In order to analyze the final number of nuclei within the progressive nucleation process, the plating time was stepwise reduced to the point shortly before the growing nuclei coalesce.

Samples plated immediately after the HF dip show a high density of nuclei. Due to the low average distance, the nuclei coalize during the first seconds of plating. Then, a homogenous layer growth is observed..

It is indicated by the chosen pictures that the number of nuclei on the oxidized surface is significantly lower. As the average distance of single nuclei is higher for Groups 2 and 3 than Group 1, it takes longer duration until a continuous layer is formed. Within the first 10 s, the nuclei grow individually. The final number of nuclei for the samples from Groups 2 and 3 is reached within 5 and 10 s. In the first instances of the plating process, nickel deposition is restricted to a smaller area for samples with oxidized surfaces, but the applied current is equal. Thus, the growth rate of the single nuclei is higher on the oxidized surfaces.

The nuclei on the sample from Group 1 show a low contact angle and a rather hemispherical shape, whereas samples from Groups 2 and 3 show high contact angles and rather spherical shapes. This matches with findings of nickel nucleation during electroplating on oxidized p-type silicon surfaces [24]. The reduced number of nuclei indicates a limited number of nucleation active sites or locally decreased deposition rates of adatoms due to the potential barrier by the surface oxides.

As the silicon surface within the laser-ablated passivation layer opening shows manifold surface features, such as laser-induced ripples or melting structures with roundish shapes, it is a challenge to identify nickel nuclei precisely. For a more detailed characterization of the distribution of the nucleation, samples from all three groups are first plated for 1 s, then nickel was chemically removed. SEM images are taken before and after the removal of nickel on the very same wafer position. Comparing both images regarding variations allows the identification of the Ni nuclei within the rough laser-structured surface. Fig. 3 shows exemplary SEM images. The first row shows samples with the nickel nuclei layer. The second row shows SEM images from the very same position after the chemical removal of nickel. The third row highlights positions that differ in the SEM images. Colored dots indicate the position and amount of nickel nuclei.

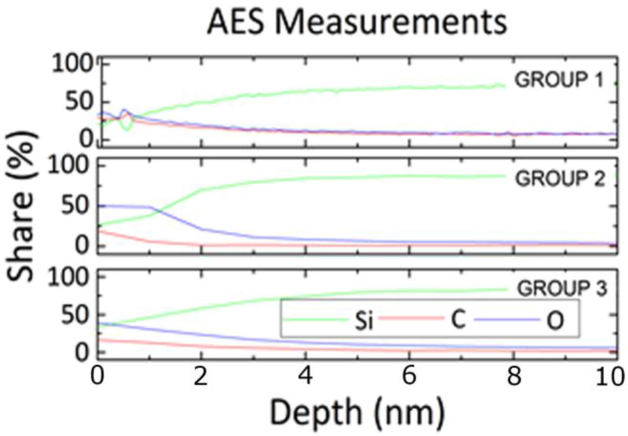

Fig. 4. Depth profiles of the elementary composition within the laser-structured passivation layer opening of samples representing the three experimental groups measured by AES.

For samples plated immediately after HF dip, the formation of nuclei seems to be increased on the pyramid tips. There seems to be no favored position for nucleation on the sample with oxidized surface. This led to the following interpretation: The nanoroughness of the surface determines the nuclei position and density. The laser-induced oxide growth is expected to be correlated to the local intensity of laser light. As more light is absorbed at pyramid tips and edges, laser-induced oxidation is expected to be more prominent at the respective positions. The removal of the silicon oxide layer during HF reveals the silicon oxide/oxide interface. The surface of silicon after oxide removal is expected to feature a nanoroughness that facilitates nickel nucleation. In contrast, a superficial (amorphous) silicon oxide layer on Groups 2 and 3 is expected to feature a smoothed-out surface without atomic edges on the sample surface. Therefore, the number of active nucleation sites is reduced.

C. Comparing AES With TEM Measurements Reveals That the Surface Oxides Are Incorporated in the Contact Stack

First, the oxide formation within the laser-structured contact openings is examined via AES before nickel deposition. By subsequent measurements and sputtering cycles, depth profiles of the chemical compositions are generated. As the excitation electron beam spot size during AES is small in respect to the diameter of a laser beam used for contact structuring, depth profiles of several positions within a single laser ablation dot are evaluated to analyze the homogeneity of the oxide formation.

Measurements were performed after laser ablation (Group 3), after an HF dip (Group 1), and after storage under ambient atmosphere (Group 2). Fig. 4 shows exemplary depth profile of the elementary composition. The carbon signal indicates the position of the adsorption layer. For Group 1, the oxygen signal follows the decay of the carbon signal that indicates both elements are present only in the adsorption layer. For Groups 2 and 3, the oxygen-related signal is increased in comparison with the carbon signal, in particular, within the first 1 nm. Thus, a surface oxide is detected after laser ablation that is dissolved by the HF dip. After storage of the sample in ambient air, a superficial oxide layer is regenerated. The sample

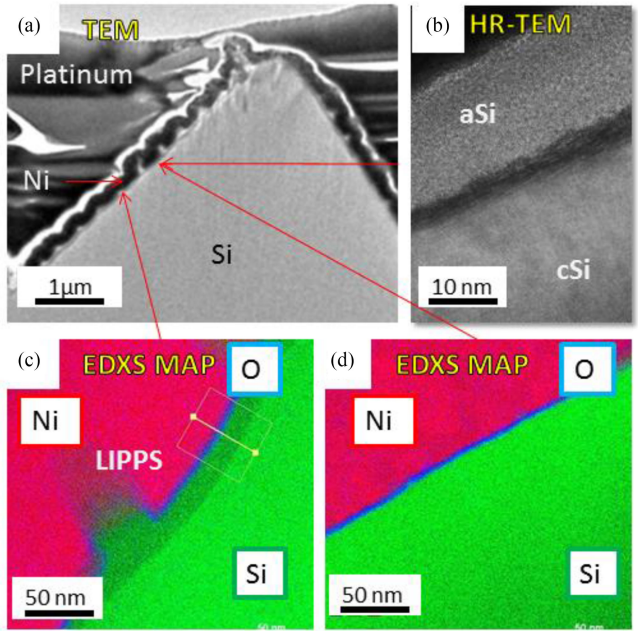

Fig. 5. High resolution transmission electron microscopy (HR-TEM) measurements of the surface near silicon volume (a) and (b). EDXS maps of a sample that was plated without the removal of the laser-induced oxides (Group 3) at two neighboring positions (c) and (d).

related to Group 2 was measured on six different pyramid tips within the passivation layer opening. On all positions, the same depth profile was measured.

TEM measurements are performed on similarly manufactured contacts after plating. Fig. 5(a) shows a representative cross section of a prepared lamella. The relevant interface is the nickel–silicon interface that features the characteristic profile-line, which is determined by laser-induced ripples. The thin silicon shreds occur equidistantly with a gap of approximately 150 nm. The TEM images further visualize the crystallinity of the surface near silicon volume. The regular ordered dots represent well-defined crystal columns (c-Si), whereas the scattered region without a defined order is related to the presence of amorphous silicon. As indicated in the close-up in Fig. 5(b), the results published by Hsiao [25] and Hermann [26] could be reproduced. Within passivation layer openings created with a UV ps-pulsed laser, the surface near silicon volume is amorphous. In particular, the laser-induced ripples were found to be consist of a-Si. The bulk silicon is crystalline. At the junction of both layers, a defect rich silicon volume is detected. This crystal configuration was found on samples from all experimental groups. In addition, measurement using Raman spectroscopy proved the presence of a-Si within the laser-structured passivation layer openings. The Raman measurements performed with a green excitation laser indicated a homogenous surface coverage with a-Si, within the respective spatial resolution of 0.5 μm.

Fig. 5(c) and (d) shows two maps indicating the elementary composition of the interface near volume for a sample from Group 3 contact as measured by EDXS. The map in Fig. 5(c) was acquired at the position of a silicon ripple. The oxygen-related signal vanishes at the tip of the riffle. This may be affected either by an inhomogeneous oxide formation or due to the sample

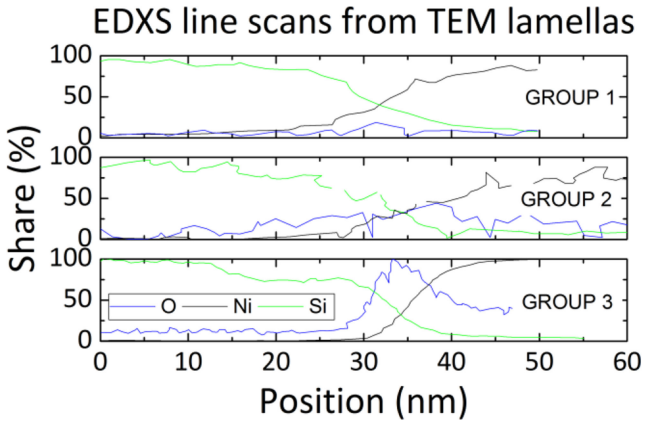

Fig. 6. EDXS line scans that indicate the elementary composition at the nickel–silicon interface. The measurements are performed on TEM lamellas.

geometry. The riffled structures are varying in thickness and height, and, thus, the material composition of the excited volume for analyzing the material composition in EDXS may be different, as estimated from the cross section of the nickel–silicon interface along the riffle. Fig. 5(d) shows the silicon–nickel interface in-between two ripples. It shows a flat silicon–nickel interface with a continuous interface oxide layer of about 4 nm in between nickel and silicon. As indicated by yellow line in Fig. 5(c), EDXS line scans were performed to quantify the layer composition. Equal line scans were performed on samples from all three groups. Fig. 6 shows the resulting profiles. All three profiles show the transition from the silicon (left) to the nickel (right) volume. The junction is blurred due to the extent of the excitation volume. At the interface, an oxide layer is detected on all three samples. For Group 1, the oxygen-related intensity is not significantly increased in proximity of the interface. For Group 2 and Group 3, an increase in the oxygen-related signal intensity is detectable close to the nickel–silicon-interface.

D. Influence of the Postplating Annealing on Interface Oxides

As already shown in previous publication and reproduced with the samples investigated in the presented article (Section III-A) the postplating annealing affects the contact resistance of plated contacts that feature an interface oxide. It is assumed that the contact resistance improvement is related to a change at the nickel–silicon interface (and not within the metal stack). Fig. 7 illustrates the composition of the interface of a plated nickel contact. The interface region is characterized by a rough (amorphous) silicon surface with an interfacial oxide layer. The interface properties are expected to be nonhomogeneous. In Section III-B, it was shown that nuclei formation during nickel deposition proceeds in homogenously. It is expected that the interface conditions vary on positions of nuclei formation (i) and the surrounding (ii) as light-induced plating requires an electron exchange between metal ions and the solar cell, the nuclei need to be electrically connected throughout the interface oxide. This may indicate that the positions of nuclei formation (region i) the electrical resistance throughout the interface layer is reduced in respect to all other positions. An improvement of the electrical

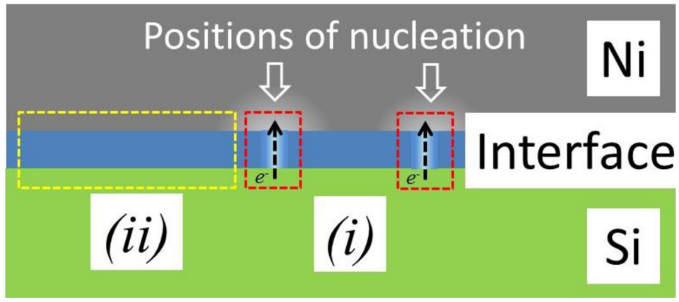

Fig. 7. Sketch of the interface situation of Ni–Cu contacts plated on an oxidized silicon surface.

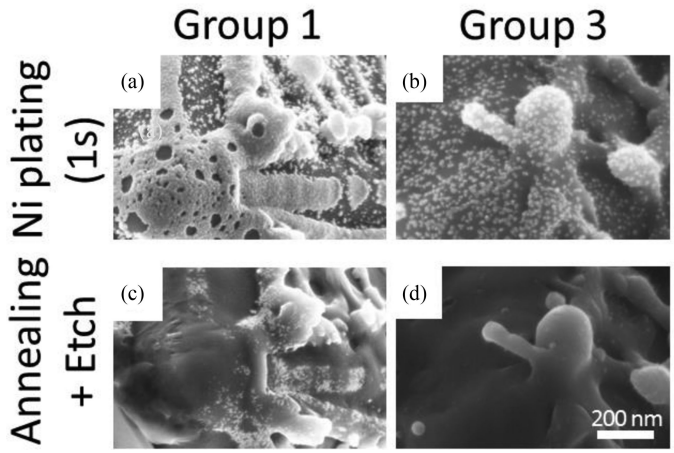

Fig. 8. SEM image within the laser-structured passivation layer opening after plated nickel for 1 s, and images taken from the same position after annealing the nickel layer and the subsequent chemical removal of unreacted nickel.

contact properties may be induced by improving the electrical contact at the position of nickel nucleation and by changing the properties of the interface oxide or the noncrystalline surface near silicon volume or by a combination of both effects.

1) Annealing Induced Changes on Ni Nuclei: An established explanation for assumption (i) is the formation of nickel silicide. The electron exchange of electrolyte and silicon bulk throughout the superficial oxide layer can be explained by interruptions or pinholes in the oxide layer. If so, silicide formation through the interruption is possible [10]. A nucleation sample was annealed using the same conditions as for the samples that showed an improved contact resistance. Subsequently, unreacted nickel was removed from the surface. Before and after annealing/metal etch SEM images are taken at the very same position. Comparing these images allows for relating positions of nuclei and silicide formation. Fig. 8(a) and (b) shows SEM images of a sample that was plated immediately after HF. The lighter gray layer in Fig. 8(a) shows the deposited nickel. In Fig. 8(c), nickel silicide structures are detected. The structures that appear bright in respect to the silicon surface are identified as silicide using EDXS. Silicides are not formed underneath all nuclei. This observation is illustrated in the shown pictures. At the tip of the pyramid [on the lower left of images in Fig. 8(a) and (c)], a dense layer of nickel is formed during nucleation, but no silicide formation is detected after annealing on the position

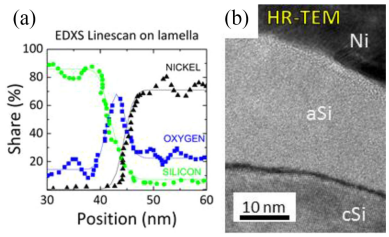

Fig. 9. (a) Evaluation of an EDXS line scan performed on a TEM lamella at the contact interface. Dotted lines represent the measured relative intensities for silicon (round), nickel (triangle), and oxygen (square). Solid lines indicate modeled intensities for a $Si/SiO_2/Ni$ interface. (b) High-resolution TEM image at the contact interface after annealing.

of the nuclei. Fig. 8(b) and (d) shows SEM images of samples with a laser-induced oxide layer. Although, a region with a dense distribution of nuclei was selected, not a single silicide structure is detected for samples of Group 3 after annealing. The typical bright silicide structures do not appear in SEM images, and in the EDXS spectra, no nickel-related signal is detected.

More general it can be stated that no modification of the silicon surface was noticed on the position of the nuclei in the SEM.

2) Annealing Induced Changes on the Interface Oxide: A change of the resistance of the interfacial layer due to the thermal treatment could be induced by changes in the crystal composition of the surface near silicon volume (for instance, due to metal-induced crystallization [27]) or by the modification of the silicon oxide layer (for instance, the formation of NiO). In order to analyze changes within the interface layers, samples with plated contacts that feature an interface oxide layer were prepared for TEM investigations and characterized in the same way as the samples presented in Section III-C. The results exhibit that the crystallinity of the surface near silicon volume is not changed by annealing, as shown in Fig. 9(b). The surface near silicon volume is characterized by amorphous silicon and a layer of defect rich silicon. In addition, in TEM investigation, no silicide formation was detected. The TEM results were complemented by spatially resolving Raman spectroscopy measurements that are performed on an equally treated sample after the chemical removal of unreacted metal. In the Raman investigation, amorphous silicon was detected before and after annealing all along the passivation layer opening. The composition of the interface oxide after annealing was investigated by EDXS. The results are equal to the ones obtained before annealing. Fig. 9(a) shows an EDXS line scan on the TEM lamella performed perpendicular to the interface. The experimental data are compared with the modeled EDXS spectra of a nickel–silicon stack with an interfacial SiO_2 layer. The accordance of modeled data (solid line) and the measurement points indicates the oxide still holds a silicon share and did not form a NiO layer by reaction with nickel. The possibility that a reaction of the interface oxide and Ni is triggered during postplating annealing is excluded by differential scanning calorimetry. A mixture of nickel powder and grounded laser-structured silicon wafer pieces was examined using the same temperature profile as during the postplating annealing. The measured calorimetry curves do not indicate a chemical reaction in between the defect rich laser-structured silicon and the nickel powder.

IV. Discussion

The presented study demonstrated that the postplating anneal affects the contact resistance of plated contacts that feature an interface oxide (Section III-A). This finding is in accordance with previous publications. It is assumed that the contact resistance improvement is related to a change at the nickel–silicon interface (and not within the metal stack). The first important result of the presented study is that *the improvement is not related to silicide growth* (for the applied thermal budget). In previous studies, the positions for the detection of silicide were chosen randomly after annealing and metal etch. Here, the nucleation was recorded and silicide growth was controlled on the position of the nuclei, but still no silicide was detected. Therefore, another mechanism is expected to cause the resistance drop. An intentionally grown native oxide (by storing the wafer for 10 min in air after the HF dip) and the laser-induced oxide during passivation layer ablation show the same characteristics: The interface oxide layer between Ni and Si is continuous even on the position of the nuclei. This might be also true for samples with HF dip. The significantly reduced silicide density compared with the Ni nuclei density indicates that a Ni diffusion barrier layer may be present even for these samples. It is assumed that nuclei can form on positions of conductive channels that allow exchange of electrons [28] but inhibit nickel diffusion and silicide formation [29]. Therefore, another mechanism might be affected by the temperature treatment (225 °C, 3 min) which causes the contact resistance improvement. The second result is that *the alternative mechanism is not related to the changes in the microstructure*—neither on the position of the nuclei nor in between the nuclei. In particular, metal-induced crystallization [27] and formation of NiO [30] can be excluded by the experimental results. The applied thermal budget in the experiments of this article (225 °C, 3 min) are significantly lower than in the respective literature.

Both results indicate that the decrease in the resistance is induced by effects related to the electron transport mechanism trough the silicon oxide layer, such as the thermal-induced formation of conductive channels in the oxide [31], [32]. Furthermore, as the laser-induced oxidation during ps-pulse UV laser treatment of a silicon surface involves photodissociation [33], rapid electron-activated oxide growth [34], and the emission of charged particles [35], the oxide may be charged. For similar metal–oxide–semiconductor stacks, it was shown that a low-temperature anneal causes a discharge of the oxides [36], which decreases the resistance. The later hypothesis was tested by rinsing the passivation layer openings in isopropanol before plating in the short duration between passivation layer ablation and plating. Interestingly, the rinsing does not decrease the resistance, but it leads to an increase in parasitic plating, equal to the HF treatment, which was not expected as isopropanol does not remove native oxides.

A debatable question is in which way the mechanism that decreases the contact resistance of the interfacial oxide layer affects the contacts plated in the standard processing route. TEM

investigation presented by Mondon *et al*. [10] already suggested that an interface oxide is also present in contact stacks plated after an HF dip. The usual HF dip was expected to result in a nonhomogeneous H-determined surface [37]. Furthermore, the high surface roughness after laser ablation and oxide removal is expected to be nonhomogenous throughout the passivation layer opening. Both might lead to a nonhomogeneous oxide formation in the initial stage after the HF dip [38]. As shown in this article, there is no complete coverage of the surface with nickel nuclei after 1 s of plating immediately after the HF dip. But there seem to be positions that are more favored for nuclei formation than others. Furthermore, the coverage with silicide after postplating annealing is even lower than the nucleation coverage. This may indicate an interfacial layer that allows electron transport but is a barrier to chemical reactions, such as a thin oxide layer. Assuming that there is a high share of oxidized surface in contacts plated according to the reference routes that includes an HF dip, a change of the electrical properties of the interfacial oxide during postplating annealing may also affect the contact resistance. This assumption motivates further studies of the effect.

V. Conclusion

The aim of the article is to investigate the microscopic basis of the contact resistance improvement induced by annealing plated contacts that feature an interface oxide layer. Therefore, three types of interfaces of laser-modified silicon and plated nickel are considered: A reference group that was plated immediately after HF dip, as in the usual production sequence for laser-structured plated contacts for silicon solar cells. A second set of samples was plated not immediately after the HF dip, but after storing the wafers 10 min in ambient air in-between HF and plating. This set of solar cells is expected to feature an interface oxide due to native oxide growth after the HF dip. The third group of samples was plated within 20 s after the laser-induced passivation layer removal without HF dip. This set of solar cells features a residual oxide layer in between laser-structured silicon and plated nickel that originates from laser-induced oxidation during passivation layer removal. After 120 s of nickel plating, homogenous nickel layers of 1 μm in thickness were observed on all three samples. However, the plating dynamics is different. On samples with native or laser-induced oxides on the surface, the nucleation differs. The amount of nucleation active sites is reduced, and the nuclei itself are characterized by a spherical shape for samples. If plating is performed immediately after the HF dip, the nuclei rather are hemispherical and densely spread on the surface. TEM investigation could reproduce that the surface near silicon volume within the passivation layer is amorphous. In particular, the laser-induced ripple structure consists of a-Si. Samples from all three groups were then characterized before and after postplating annealing. Modifications in the microstructure were examined at the position of the nickel nuclei from top-view perspective in the SEM and on arbitrary positions in-between the nuclei from cross section perspective in the TEM. It was shown that on solar cell contacts that are plated immediately after the HF dip, silicide formation is observed. But the silicide formation is limited to the points of nucleation. Furthermore, silicide is not formed at all points of nucleation. This indicates an interface barrier layer that allows electron transport but hinders chemical reaction. No silicide formation was detected on samples with interfacial oxide layers. The TEM investigations proved that the chemical composition of the interfacial silicon oxide layer is not changed during annealing. Furthermore, the crystallinity of the surface near silicon volume is not modified. Improvements of the contact resistance therefore could not be related to changes in the microstructure. It is expected that the transport mechanism of electrons throughout the interfacial oxide layer is improved during annealing. For instance, a shift of the trap-level energy of defects in the oxide could cause the observed effect. Considering that oxide layer is reported to be inherent in plated contacts, the formation of the oxide layer needs to be understood in more detail to set new target for the optimization of temperature profiles during postplating annealing. Furthermore, the results motivate to study new postplating treatments, such as current pulses that also may modify the electron transport mechanism of interfacial oxide layers.

References

[1] A. Mette *et al.*, "Increasing the efficiency of screen-printed silicon solar cells by light-induced silver plating," in *Proc. IEEE 4th World Conf. Photovolt. Energy Conf.*, Waikoloa, HI, USA, 2006, pp. 1056–1059.

[2] D. Pysch *et al.*, "Pilot production of highly efficient metal catalyzed textured diamond wire sawn mc-Si solar cells combined with nickel–copper plated front contact processing," *Energy Procedia*, vol. 130, pp. 14–22, 2017.

[3] A. Ciesla *et al.*, "High-voltage p-type PERC solar cells with anchored plating and hydrogenation," *Prog. Photovolt. Res. Appl.*, vol. 26, no. 6, pp. 397–401, 2018.

[4] J. T. Horzel *et al.*, "Industrial Si solar cells with Cu-based plated contacts," *IEEE J. Photovolt.*, vol. 5, no. 6, pp. 1595–1600, Nov. 2015.

[5] S. Kluska *et al.*, "Plated fine line metallization for PERC solar cells," in *Proc. 33th Eur. Photovolt. Sol. Energy Conf. Exhib.*, Bruxelles, Belgium, 2018.

[6] E. Cornagliotti *et al.*, "High efficiency bifacial n-PERT cells with co-plated Ni/Ag contacts for multi-wire interconnection," *Energy Procedia*, vol. 130, pp. 50–54, 2017.

[7] G. Cimiotti, J. Bartsch, A. Kraft, A. Mondon, and M. Glatthaar, "Design rules for solar cells with plated metallization," *Energy Procedia*, vol. 67, pp. 84–92, Apr. 2015.

[8] J. Bonse *et al.*, "Applications of laser-induced periodic surface structures (LIPSS)," *Proc SPIE*, vol. 10092, 2017, Art. no. 100920N.

[9] X. Wang *et al.*, "Monitoring of adhesion for plated metallisation: Why busbar pull tests are not sufficient," *Energy Procedia*, vol. 92, pp. 978–983, Aug. 2016.

[10] A. Mondon *et al.*, "Nanoscale investigation of the interface situation of plated nickel and thermally formed nickel silicide for silicon solar cell metallization," *Appl. Surf. Sci.*, vol. 323, pp. 31–39, Dec. 2014.

[11] C. M. Liu, W. L. Liu, S. H. Hsieh, T. K. Tsai, and W. J. Chen, "Interfacial reactions of electroless nickel thin films on silicon," *Appl. Surf. Sci.*, vol. 243, no. 1–4, pp. 259–264, Apr. 2005.

[12] S. Kluska *et al.*, "Easy plating—A simple approach to suppress parasitically metallized areas in front side Ni/Cu plated crystalline Si solar cells," *IEEE J. Photovolt.*, vol. 7, no. 5, pp. 1270–1277, Sep. 2017.

[13] M. Heinrich *et al.*, "Quantification of front side metallization area on silicon wafer solar cells for background plating detection," *Energy Procedia*, vol. 77, pp. 717–724, 2015.

[14] S. Braun, A. Zuschlag, B. Raabe, and G. Hahn, "The origin of background plating," *Energy Procedia*, vol. 8, pp. 565–570, 2011.

[15] M. S. Jeong, K. H. Min, M. G. Kang, J. I. Lee, and H.-E. Song, "Control of ghost plating by antireflection coating layer stacking on crystalline silicon solar cells," in *Proc. IEEE 43rd Photovolt. Spec. Conf.*, Portland, OR, USA, 2016, pp. 2910–2912.

[16] B. Grübel *et al.*, "Easy plating—Study on contact interface properties of parasitic plating-free Ni/Cu solar cells," in *Proc. 32th Eur. Photovolt. Sol. Energy Conf. Exhib.*, Amsterdam, The Netherlands, 2017. [Online]. Available: https://www.ise.fraunhofer.de/content/dam/ise/de/documents/publications/conference-paper/33-eupvsec-2017/Gr%C3%BCbel_2CV282.pdf

[17] M. C. Raval *et al.*, "Study of nickel silicide formation and associated fill-factor loss analysis for silicon solar cells with plated Ni-Cu based metallization," *IEEE J. Photovolt.*, vol. 5, no. 6, pp. 1554–1562, Nov. 2015.

[18] A. Mondon *et al.*, "Nanoscale investigation of the interface situation of plated nickel and thermally formed nickel silicide for silicon solar cell metallization," *Appl. Surf. Sci.*, vol. 323, pp. 31–39, 2014.

[19] M. Morita, T. Ohmi, E. Hasegawa, M. Kawakami, and M. Ohwada, "Growth of native oxide on a silicon surface," *J. Appl. Phys.*, vol. 68, no. 3, pp. 1272–1281, 1990.

[20] A. Büchler *et al.*, "How to realize solar cells with laser structured plated Ni-Cu-contacts with excellent adhesion and high fill-factors without parasitic plating," *Proc. IEEE 44th Photovolt. Spec.*, 2017, pp. 884–887.

[21] A. Büchler *et al.*, "Interface oxides in femtosecond laser structured plated Ni–Cu–Ag contacts for silicon solar cells," *Sol. Energy Mater. Sol. Cells*, vol. 166, pp. 197–203, 2017.

[22] A. Mondon, "Nickel silicide from plated nickel for high adhesion of fully palted silicon solar cell metallization," Ph.D. thesis, Rochester Inst. Technol., Rochester, NY, USA, 2015.

[23] J. Rodriguez, W. Zhang, S. Lim, and A. Lennon, "Improved metal adhesion with galvanic nickel plating to silicon solar cells," *Sol. Energy Mater. Sol. Cells*, vol. 165, pp. 17–26, 2017.

[24] P.-C. Hsiao *et al.*, "266-nm ps laser ablation for copper-plated p-type selective emitter PERC silicon solar cells," *IEEE J. Photovolt.*, vol. 8, no. 4, pp. 952–959, Jul. 2018.

[25] H. Philipsen *et al.*, "Nucleation and growth kinetics of electrodeposited Ni films on Si(100) surfaces," *Electrochim. Acta*, vol. 230, pp. 407–417, 2017.

[26] S. Hermann *et al.*, "Impact of surface topography and laser pulse duration for laser ablation of solar cell front side passivating SiN_x layers," *J. Appl. Phys.*, vol. 108, no. 11, 2010, Art. no 114514.

[27] S. Y. Yoon, K. H. Kim, C. O. Kim, J. Y. Oh, and J. Jang, "Low temperature metal induced crystallization of amorphous silicon using a Ni solution," *J. Appl. Phys.*, vol. 82, no. 11, pp. 5865–5867, 1997.

[28] J. G. Simmons, "Conduction in thin dielectric films," *J. Phys. D, Appl. Phys.*, vol. 4, no. 5, p. 613, 1971.

[29] J. T. Mayer, R. F. Lin, and E. Garfunkel, "Surface and bulk diffusion of adsorbed nickel on ultrathin thermally grown silicon dioxide," *Surf. Sci.*, vol. 265, no. 1-3, pp. 102–110, 1992.

[30] M. Zöllner, S. Kipp, and K. D. Becker, "Reactive processes of nickel oxide on oxidic substrates as observed by scanning force microscopy," *Cryst. Res. Technol.*, vol. 35, no. 3, pp. 299–306, 2000.

[31] J. Joshua Yang *et al.*, "The mechanism of electroforming of metal oxide memristive switches," *Nanotechnology*, vol. 20, no. 21, 2009, Art. no. 215201.

[32] G. Dearnaley, Am Stoneham, and D. V. Morgan, "Electrical phenomena in amorphous oxide films," *Rep. Prog. Phys.*, vol. 33, no. 3, pp. 1129–1191, 1970.

[33] T. E. Orlowski and D. A. Mantell, "Ultraviolet laser-induced oxidation of silicon: The effect of oxygen photodissociation upon oxide growth kinetics," *J. Appl. Phys.*, vol. 64, no. 9, pp. 4410–4414, 1988.

[34] E. M. Young, "Electron-active silicon oxidation," *Appl. Phys. A*, vol. 47, no. 3, pp. 259–269, 1988.

[35] J. M. Liu, R. Yen, H. Kurz, and N. Bloembergen, "Phase transformation on and charged particle emission from a silicon crystal surface, induced by picosecond laser pulses," *Appl. Phys. Lett.*, vol. 39, no. 9, pp. 755–757, 1981.

[36] H. C. Card, "Aluminum–silicon schottky barriers and ohmic contacts in integrated circuits," *IEEE Trans. Electron Devices*, vol. 23, no. 6, pp. 538–544, Jun. 1976.

[37] W. Henrion, M. Rebien, H. Angermann, and A. Röseler, "Spectroscopic investigations of hydrogen termination, oxide coverage, roughness, and surface state density of silicon during native oxidation in air," *Appl. Surf. Sci.*, vol. 202, no. 3-4, pp. 199–205, 2002.

[38] S. Watanabe, N. Nakayama, and T. Ito, "Homogeneous hydrogen-terminated Si(111) surface formed using aqueous HF solution and water," *Appl. Phys. Lett.*, vol. 59, no. 12, pp. 1458–1460, 1991.